


Article

Characterization of Tungstates of the Type $\text{Hf}_{1-x}\text{Ln}_x\text{W}_2\text{O}_{8-x/2}$ ($\text{Ln} = \text{Eu}, \text{Tm}, \text{Lu}$) Synthesized Using the Hydrothermal Method

Martin Tsvetkov ^{1,*} , Martin Nedyalkov ¹, Evgenia Valcheva ² and Maria Milanova ^{1,*}

¹ Laboratory of Rare and Rare Earth Elements, Department of Inorganic Chemistry, Faculty of Chemistry and Pharmacy, University of Sofia “St. Kliment Ohridski”, 1, J. Bourchier, 1164 Sofia, Bulgaria; martin_nedyalkov_rze@abv.bg

² Department of Condensed Matter Physics and Microelectronics, Faculty of Physics, University of Sofia “St. Kliment Ohridski”, 3, J. Bourchier, 1164 Sofia, Bulgaria; epv@phys.uni-sofia.bg

* Correspondence: nhmt@chem.uni-sofia.bg (M.T.); nhmm@chem.uni-sofia.bg (M.M.)

Abstract: Pure HfW_2O_8 - and Ln^{3+} -containing solid solutions, $\text{Hf}_{1-x}\text{Ln}_x\text{W}_2\text{O}_{8-x/2}$ ($\text{Ln} = \text{Eu}, \text{Tm}, \text{Lu}$), were synthesized using the hydrothermal method. The lanthanide ions were selected based on the differences between their ionic radii. A content of the Ln^{3+} ions in the range of 0.01–0.15 mol with a step of 0.02 was used for $\text{Hf}_{1-x}\text{Ln}_x\text{W}_2\text{O}_{8-x/2}$ preparation, although the main research was performed on $x = 0.01$ and 0.05 samples because of an inhomogeneity detected by powder X-ray diffraction (XRD) when the content of Ln^{3+} was above 0.07–0.09 mol. X-ray diffraction measurements were supported by Raman and infrared spectroscopy. A new band in the Raman spectra of the samples with 0.05 mol Ln^{3+} , as well as a red shift of the most intensive band (assigned to valence stretching of W–O–W bonds) as a result of the Ln^{3+} presence, was detected. The Scanning Electron Microscopy and Transmission Electron Microscopy micrographs revealed well-crystallized microcrystals with lengths in the range of 2–5 μm , with larger interplanar distances, measured in the solid solutions of the same crystal plain. The $\alpha\text{-HfW}_2\text{O}_8 \rightarrow \beta\text{-HfW}_2\text{O}_8$ order-to-disorder phase transition was followed by high temperature XRD, and its reversibility was evident. The influence of the Ln^{3+} both on the unit cell parameters of the solid solutions and on the temperature of phase transition and on the coefficient of thermal expansion, CTE, was observed. A band gap energy in the range of 2.8–3.1 eV for pure HfW_2O_8 and for the solid solutions $\text{Hf}_{1-x}\text{Ln}_x\text{W}_2\text{O}_{8-x/2}$ ($x = 0.01$ and 0.05) was determined.

Keywords: hafnium tungstate; lanthanide ions; high-temperature XRD; Raman spectroscopy; FT-IR spectroscopy; electron microscopy; order–disorder phase transition; negative coefficient of thermal expansion; band gap energy



Citation: Tsvetkov, M.; Nedyalkov, M.; Valcheva, E.; Milanova, M. Characterization of Tungstates of the Type $\text{Hf}_{1-x}\text{Ln}_x\text{W}_2\text{O}_{8-x/2}$ ($\text{Ln} = \text{Eu}, \text{Tm}, \text{Lu}$) Synthesized Using the Hydrothermal Method. *Crystals* **2022**, *12*, 327. <https://doi.org/10.3390/cryst12030327>

Academic Editor: Shujun Zhang

Received: 1 February 2022

Accepted: 23 February 2022

Published: 26 February 2022

Publisher’s Note: MDPI stays neutral with regard to jurisdictional claims in published maps and institutional affiliations.



Copyright: © 2022 by the authors. Licensee MDPI, Basel, Switzerland. This article is an open access article distributed under the terms and conditions of the Creative Commons Attribution (CC BY) license (<https://creativecommons.org/licenses/by/4.0/>).

1. Introduction

Materials which contract upon heating, i.e., with negative thermal expansion (NTE), can play the role of thermal-expansion compensators, so they are considered important in the development of composites with adjustable thermal expansion [1–3]. Examples of these materials include various silicates [4], cyanide-bridged compounds [5], nickel-based perovskite oxide [6], and many others, reviewed in [7]. The isostructural tungstates from the group of the cubic AW_2O_8 , $\text{A} = \text{Zr}, \text{Hf}$ [8], are among these materials. The cubic AW_2O_8 have an open framework structure with WO_4 tetrahedra sharing three of their four oxygen atoms with the adjacent AO_6 octahedra [1,2,8–10]. ZrW_2O_8 , as well as HfW_2O_8 , shows an exceptionally large isotropic negative thermal expansion over an exceptionally large temperature range (0.3–1050 K) [8]. ZrW_2O_8 goes through an order–disorder change at about 440 K (167 °C) from a metastable, low-temperature cubic phase (alpha) with a coefficient of NTE of $-9 \times 10^{-6} \text{ K}^{-1}$ to a metastable, high temperature cubic phase (beta) with a coefficient of NTE of $-5 \times 10^{-6} \text{ K}^{-1}$ [8,10]. The NTE for HfW_2O_8 is less pronounced in the alpha-phase ($-9 \times 10^{-6} \text{ K}^{-1}$) than in beta-phase ($-6 \times 10^{-6} \text{ K}^{-1}$) with a temperature of order/disorder phase transition of 463 K [11], i.e., the absolute

thermal expansion coefficient is slightly smaller for HfW_2O_8 than for ZrW_2O_8 . Calorimetric studies show that the phase transition temperature is 24 K higher for HfW_2O_8 than for ZrW_2O_8 , which is probably due to the stronger chemical bond of Hf-O than Zr-O [12]. In any case, ZrW_2O_8 and HfW_2O_8 show the low-high symmetry phase transition at similar temperatures and similar thermal contraction properties [9]. A phase transition from an alpha-phase to an orthorhombic gamma-phase induced under compression in both ZrW_2O_8 and HfW_2O_8 has been observed; significantly higher pressures are required to induce the transition in HfW_2O_8 than in ZrW_2O_8 [11]. The NTEs of those compounds originate from lattice vibrations, which could be affected by the masses and ionic radii of the constituent atoms [13]. The introduction of ions with different radii and charges can lead to a disorder in the crystalline structure of the tungstates and, consequently, to changes in their properties as detected by us for limited concentration ranges of Eu(III) on NTE and the phase transformation temperatures of ZrW_2O_8 [14]. The introduction of M^{4+} , like Sn^{4+} and Ti^{4+} in tungstates [15,16], as well as the insertion of Y^{3+} and Lu^{3+} in HfW_2O_8 , have been studied [17,18]. It has been found that even small amounts can lead to essential changes in the temperatures of phase transitions, for instance, a 4% replacement decreases the temperature of the transition to 390 K for Y^{3+} , 380 K for In^{3+} and 360 K for Sc^{3+} [17–19]. A series of solid solutions with a cubic ZrW_2O_8 structure, where the crystal sites of Zr^{4+} are substituted partially by lanthanide cations Ln^{3+} ($\text{Ln} = \text{Yb}, \text{Er}, \text{Eu}$), have been studied, and it has been found that the solubility of lanthanide cations in $\text{Zr}_{1-x}\text{Ln}_x\text{W}_2\text{O}_{8-x/2}$ solid solutions increases as the radius of the lanthanide cations decrease [20]. In an attempt to expand the research, in this work, the influence of lanthanide ions Eu^{3+} , Tm^{3+} , and Lu^{3+} on the properties of HfW_2O_8 was followed by synthesis and characterization of solid solutions of the type $\text{Hf}_{1-x}\text{Ln}_x\text{W}_2\text{O}_{8-x/2}$.

2. Materials and Methods

$\text{HfOCl}_2 \cdot 2\text{H}_2\text{O}$ (Sigma-Aldrich Chemie GmbH, Taufkirchen, Germany) and $\text{Na}_2\text{WO}_4 \cdot 2\text{H}_2\text{O}$ (Aldrich Chemie GmbH, Taufkirchen, Germany) (both ACS grade) were used as starting materials. The nitrates $\text{Ln}(\text{NO}_3)_3 \cdot n\text{H}_2\text{O}$ were synthesized using Eu_2O_3 (Fluka Chemie GmbH, Buchs, Switzerland, p.a.), Tm_2O_3 (Sigma Aldrich, 99.99% Sigma-Aldrich Chemie GmbH, Taufkirchen, Germany), and Lu_2O_3 (Sigma Aldrich, 99.99% Sigma-Aldrich Chemie GmbH, Taufkirchen, Germany) by dissolving them in heated diluted HNO_3 (70%, Sigma-Aldrich Chemie GmbH, Taufkirchen, Germany), followed by crystallization after the cooling of the solution. Titration with a 0.01 M water solution of a di-sodium salt of ethylene diammine tetraacetic acid Na_2EDTA (99%+, Sigma-Aldrich Chemie GmbH, Taufkirchen, Germany) was applied to determine the amount of crystallization water in the nitrates synthesized.

The synthesis of HfW_2O_8 : The initial water solutions of $\text{HfOCl}_2 \cdot 2\text{H}_2\text{O}$ (8.5 mL, 0.1 M) and Na_2WO_4 (8.5 mL, 0.1 M) were prepared with a calculated stoichiometric ratio of $\text{Hf}/\text{W} = 1:2$. The two solutions were added dropwise to 15 mL of distilled water simultaneously through dropping funnels. After mixing, the new solution (the white suspension) obtained was heated at 60 °C and stirred for 30 min. To obtain a homogeneous solution, 15 mL of 6 M HCl (37%, Sigma-Aldrich Chemie GmbH, Taufkirchen, Germany) was added (in order to obtain the final concentration of HCl about 3 M). An additional heating at 60 °C for 2 h was applied followed by adding of 5 mL 1-butanol. The solution obtained was heated in a 75 mL Teflon autoclave for 15 h at 180 °C, while stirring. Then, the obtained suspension was cooled down to room temperature followed by filtering, washing with water and ethyl alcohol, and drying at 50 °C. After calcination in preheated furnace for 1 h at 600 °C, the sample of HfW_2O_8 was analyzed and characterized.

The synthesis of the solid solutions: The procedure presented above for the pure HfW_2O_8 was followed for the synthesis of solid solutions, with only the exception of the first step, where a solution of $\text{Ln}(\text{NO}_3)_3 \cdot n\text{H}_2\text{O}$ was added to obtain $\text{Hf}_{1-x}\text{Ln}_x\text{W}_2\text{O}_{8-x/2}$ samples. The amount of the Ln^{3+} ($\text{Ln} = \text{Eu}, \text{Tm}, \text{Lu}$) ions used was in the range of 0.01–0.15 mol with a step of 0.02. The scheme for the typical synthesis procedure applied is presented in Figure 1.

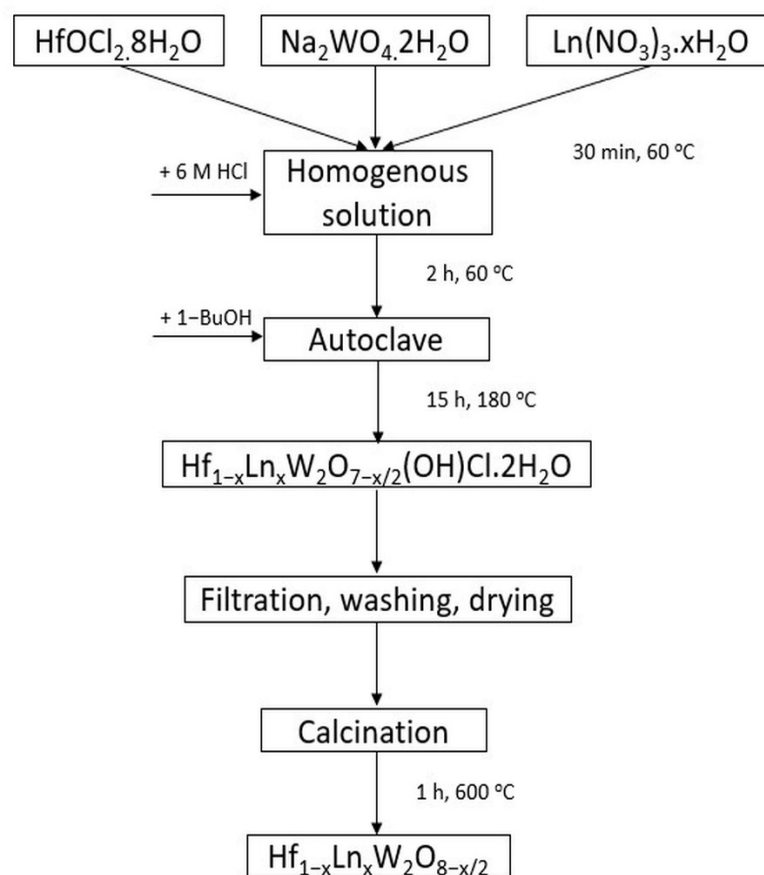


Figure 1. Typical synthesis steps.

The methods for characterization were as follows. A high temperature XRD was performed using a PANalytical Empyrean diffractometer (Malvern PANalytical Empyrean, Almelo, Netherlands) with a PIXcel 3D detector. The XRD patterns were recorded between $15\text{--}90^\circ$ 2θ with a step of 0.026° . An Anton Paar HTK 16N camera (Anton Paar GmbH, Graz, Austria) was used for in situ high-temperature measurements in the interval of $25\text{--}250^\circ\text{C}$ with different steps. The unit cell parameters were calculated using the Rietveld method using the FullProf Suite software (v01-2021, Grenoble, France) [21]. Raman spectroscopy: The measurements were carried out on a HORIBA Jobin Yvon Labram HR 800 micro-Raman spectrometer (Horiba, Piscataway, NJ, USA) with a He–Ne (633 nm) laser, the absolute measurement accuracy of which was 0.5 cm^{-1} or better. FT-IR spectroscopy: The measurements were performed on a FT-IR Nicolet 6700—Thermo Scientific (Waltham, MA, USA). UV–Vis absorption spectroscopy was applied using an Evolution 300 UV–Vis spectrometer (Thermo Scientific, Waltham, MA, USA) to measure the absorption in the range of $200\text{--}900\text{ nm}$. Transmission Electron Microscopy, TEM: investigations were performed on a JEM 2100 (JEOL, Tokyo, Japan) transmission electron microscope with an accelerator voltage of 200 kV and up to $1,500,000$ times magnification. SEM: A Hitachi TM4000 (Krefeld, Germany) was used, with an accelerating voltage 15 kV .

3. Results

3.1. XRD of $\alpha\text{-HfW}_2\text{O}_8$ and $\beta\text{-HfW}_2\text{O}_8$

The structures of $\alpha\text{-HfW}_2\text{O}_8$ and $\beta\text{-HfW}_2\text{O}_8$ were needed to evaluate the structure of the solid solutions. As long as our ICSD database did not contain .cif files of the $\alpha\text{-HfW}_2\text{O}_8$ nor $\beta\text{-HfW}_2\text{O}_8$, we used the .cif file for $\alpha\text{-ZrW}_2\text{O}_8$ (ICSD PDF #50-1868) to present the structure of $\alpha\text{-HfW}_2\text{O}_8$, which is isostructural to $\alpha\text{-HfW}_2\text{O}_8$. As for $\beta\text{-HfW}_2\text{O}_8$, the .cif file of $\text{ZrW}_{0.977}\text{Mo}_{1.023}\text{O}_8$ (ICSD PDF #01-070-6112), which is isostructural to $\beta\text{-ZrW}_2\text{O}_8$ and $\beta\text{-HfW}_2\text{O}_8$, was used [22]. The diffractograms of the low-temperature phase ($\alpha\text{-HfW}_2\text{O}_8$)

and the high-temperature phase (β -HfW₂O₈) synthesized using the hydrothermal method along with mentioned ICSD data are shown in Figure 2. The starting structural parameters used for α -HfW₂O₈ and β -HfW₂O₈ are listed in Tables S1 and S2.

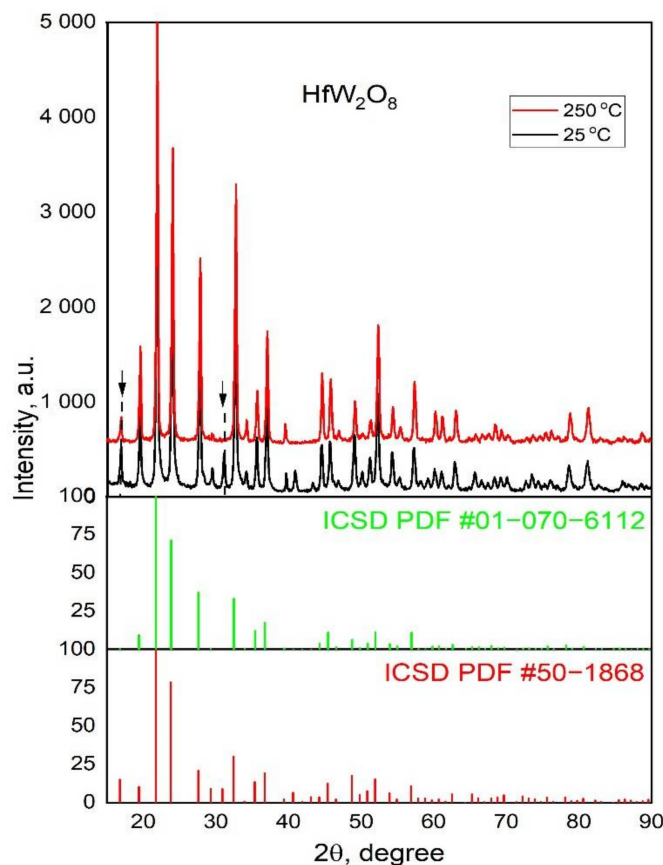


Figure 2. The comparison of XRD data for the synthesized α -HfW₂O₈ and β -HfW₂O₈ (top) with the analogues of the ICSD data for α -ZrW₂O₈ (bottom), ZrW_{0.977}Mo_{1.023}O₈ (middle).

3.2. Characterization of the Solid Solutions Hf_{1-x}Ln_xW₂O_{8-x/2} by XRD; Raman and IR Spectroscopy—Homogeneity of the Samples; Influence of Ln³⁺

By introducing Ln³⁺ ions to the structure of HfW₂O₈ oxygen vacancies were generated, leading to the general formula of our solid solutions, i.e., Hf_{1-x}Ln_xW₂O_{8-x/2}. It is widely accepted that O-vacancies introduced in this way are considered intrinsic, but we did not follow their evolution, nor did we have a way to measure them exactly. Essential to point out is that, during the Rietveld refinement, the occupancy of all O-atoms was refined, but, due to the very low concentration of these defects, we did not notice any major deviations.

The powder X-ray diffraction patterns of the solid solutions evidenced their crystalline nature. All diffractograms show the reflection peaks typical for HfW₂O₈. XRD patterns of the samples Hf_{1-x}Eu_xW₂O_{8-x/2}, 0.01 ≤ x ≤ 0.15, recorded at 25 °C, are presented in Figure 3. The reflexes observed in the samples of Hf_{1-x}Eu_xW₂O_{8-x/2} with x = 0.09 and up to x = 0.15 indicate the formation of a secondary WO₃ phase. Based on that, it can be stated that the samples of Hf_{1-x}Ln_xW₂O_{8-x/2} obtained were phase-homogeneous up to x = 0.07, as shown by the powder XRD patterns of Hf_{1-x}Eu_xW₂O_{8-x/2}. Considering that, we focus our further research mainly on the solid solutions Hf_{1-x}Ln_xW₂O_{8-x/2} with x 0.01 and 0.05.

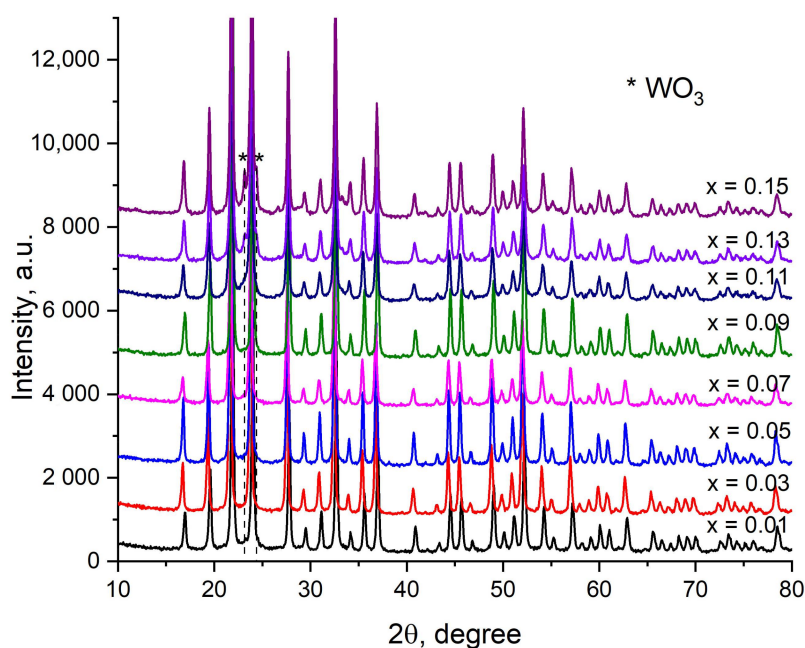


Figure 3. XRD patterns of the solid solutions $\text{Hf}_{1-x}\text{Eu}_x\text{W}_2\text{O}_{8-x/2}$, $0.01 \leq x \leq 0.15$, recorded at 25 °C.

Taking into account that Raman spectroscopy is known as an effective and sensitive method to track the changes in the position and bonding between the atoms of W and O in the crystal lattice [23], Raman spectra were recorded for the pure $\alpha\text{-HfW}_2\text{O}_8$ and the solid solutions $\text{Hf}_{1-x}\text{Ln}_x\text{W}_2\text{O}_{8-x/2}$, $x = 0.01$ and 0.05 . The structure of $\alpha\text{-HfW}_2\text{O}_8$ is viewed as a network of corner-sharing HfO_6 octahedra and WO_4 tetrahedra, and the Raman modes of tungstates are assigned as lattice modes, translation, vibrational, and internal modes of WO_4 in the range of $100\text{--}1,100\text{ cm}^{-1}$ [24,25]. In the Raman spectrum of the pure $\alpha\text{-HfW}_2\text{O}_8$ bands, low- and high-wavenumbers, in the range of $400\text{--}100$ and $1,040\text{--}700\text{ cm}^{-1}$ are observed (Figure 4). The precise values of the bands position are listed in Table S3.

The Raman spectra interpretation was based on the literature data [26]. The modes centered at $1,026$, 999 , 921 , 896 , and 859 cm^{-1} can be assigned to the symmetric stretching vibrations vs. modes of the WO_4 ; the modes of 796 , 746 to the WO_4 asymmetric stretching (ν_{as} modes); the one at 373.03 to the asymmetric bending, 345.9 , 322.8 ; and 297.1 cm^{-1} to the symmetric bending modes. The bands at 199 and 125 cm^{-1} are regarded as originating from lattice modes.

In the Raman spectra of the solid solutions $\text{Hf}_{1-x}\text{Ln}_x\text{W}_2\text{O}_{8-x/2}$, a shifting of bands toward higher wavenumbers, i.e., higher frequencies, is observed (Figure 4a,b). This shifting affects the bands assigned to the stretching vibrations of $\text{W}\text{--}\text{O}\text{--}\text{W}$ bonds, $\nu_{\text{s}}(\text{WO}_4)$, namely, 795.5 cm^{-1} (the most intensive one) and 745.9 cm^{-1} (the weaker one) of HfW_2O_8 . Both bands are shifted to higher wavenumbers, i.e., $812\text{--}813$ and $764\text{--}765\text{ cm}^{-1}$, respectively, in the solid solutions $\text{Hf}_{1-x}\text{Ln}_x\text{W}_2\text{O}_{8-x/2}$, $x = 0.01$ and $x = 0.05$ (Figure 4a,b). Additionally, new bands at 721 , 723 , and 693 cm^{-1} were detected in the spectra of $\text{Hf}_{0.95}\text{Ln}_{0.05}\text{W}_2\text{O}_{8-x/2}$, $\text{Ln} = \text{Eu}$, Tm , and Lu , respectively. At the same time, the shifting of the band at $1,025.98\text{ cm}^{-1}$ for pure $\alpha\text{-HfW}_2\text{O}_8$ toward the higher wavenumber of $1,043\text{ cm}^{-1}$ for $\text{Hf}_{0.99}\text{Ln}_{0.01}\text{W}_2\text{O}_{8-x/2}$ and $\text{Hf}_{0.95}\text{Ln}_{0.05}\text{W}_2\text{O}_{8-x/2}$ is clear evidence of the influence of Ln^{3+} on the crystal structure. Regarding the position of the band, the influence of Ln^{3+} is expressed by the essential decreasing of the intensity of the band in question, $1,043\text{ cm}^{-1}$, for the samples $\text{Hf}_{0.95}\text{Ln}_{0.05}\text{W}_2\text{O}_{8-x/2}$, i.e., the effect of the incorporation of the larger amount of Ln^{3+} is detected.

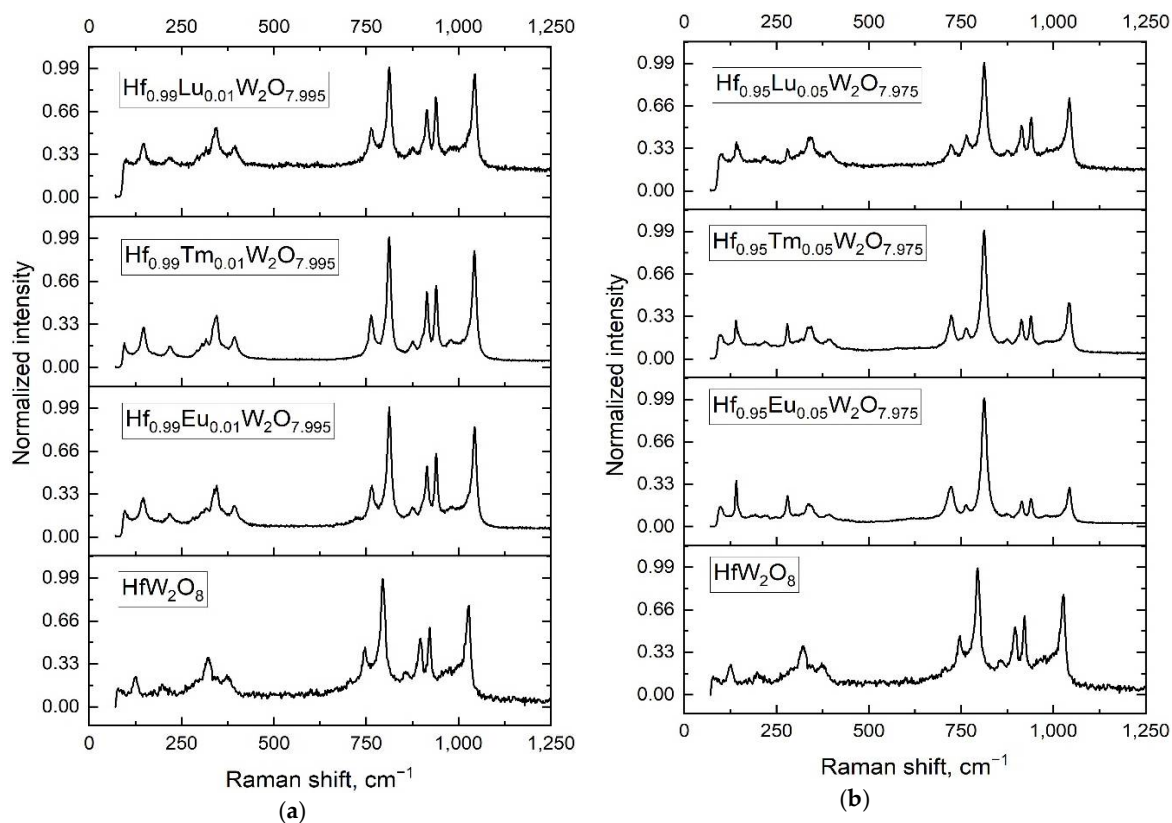


Figure 4. Raman spectra of HfW_2O_8 and $\text{Hf}_{1-x}\text{Ln}_x\text{W}_2\text{O}_{8-x/2}$, (a) $x = 0.01$ and (b) $x = 0.05$.

In addition to the Raman, infrared spectra of the samples were recorded in the range of $4,000\text{--}400\text{ cm}^{-1}$, with easily noticeable bands showing the presence of water (Figure S1). The more informative range of $1,100\text{--}400\text{ cm}^{-1}$, with the absorption bands of 941 , 917 , 882 , 832 , 809 , 777 , and 761 cm^{-1} accentuated with dashed lines, are shown in Figure 5.

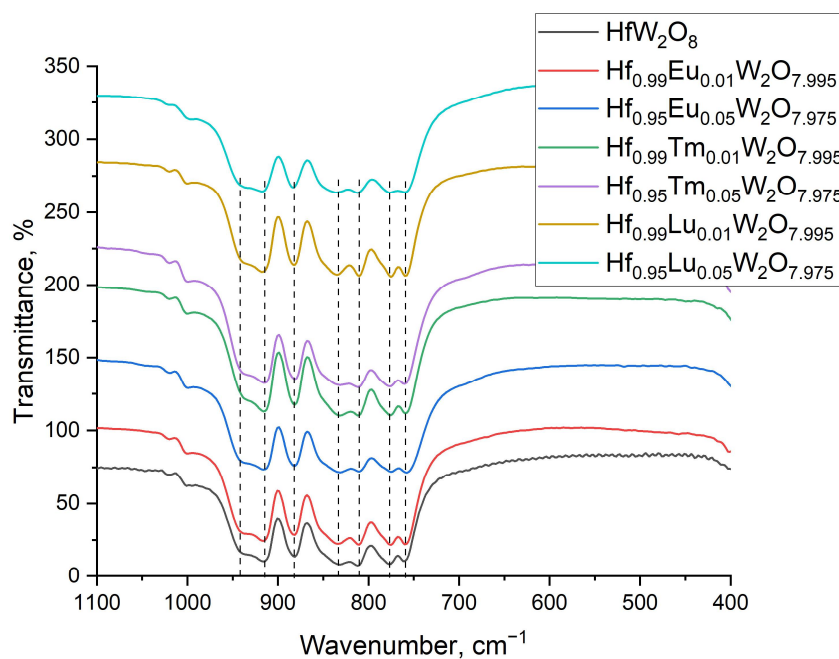


Figure 5. FT-IR spectra of the samples in the range of $1100\text{--}400\text{ cm}^{-1}$.

The bands are caused by the symmetric (941, 917, 882, and 832 cm^{-1}) and asymmetric stretching vibrations of W-O in WO_4 tetrahedra (809, 777, and 761 cm^{-1}) [26]. The asymmetric and symmetric bending, as well as the lattice modes, were below 400 cm^{-1} , and so, they were not detected by the FT-IR equipment used. The influence of the Ln^{3+} doping is revealed in the spectrum of $\text{Hf}_{0.95}\text{Lu}_{0.05}\text{W}_2\text{O}_{8-x/2}$, where a broadening of the band at 761 cm^{-1} is visible, although slightly noticeable in the spectra of the other $\text{Hf}_{0.95}\text{Ln}_{0.05}\text{W}_2\text{O}_{8-x/2}$.

3.3. The Morphology of the Samples by Electron Microscopy, SEM, and TEM

The SEM micrographs exhibit similar needle-like crystals of HfW_2O_8 (Figure 6a) and of the solid solutions $\text{Hf}_{0.99}\text{Eu}_{0.01}\text{W}_2\text{O}_{8-x/2}$ and $\text{Hf}_{0.995}\text{Eu}_{0.005}\text{W}_2\text{O}_{8-x/2}$ (Figure 6b,c), proving that the morphology is not affected by Ln^{3+} . SEM micrographs of the precursor $\text{HfW}_2\text{O}_7(\text{OH;Cl})_2$ and $\alpha\text{-HfW}_2\text{O}_8$ verifying the method of $\alpha\text{-HfW}_2\text{O}_8$ formation are shown in Figure S2.

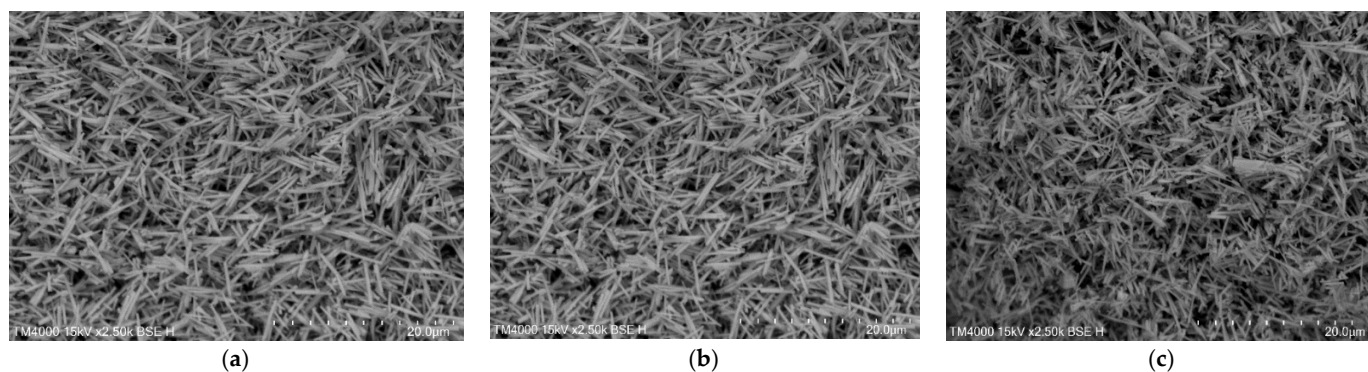


Figure 6. SEM micrographs of (a) HfW_2O_8 , (b) $\text{Hf}_{0.99}\text{Eu}_{0.01}\text{W}_2\text{O}_{7.995}$, and (c) $\text{Hf}_{0.995}\text{Eu}_{0.005}\text{W}_2\text{O}_{7.975}$.

The needle-like microcrystals, similar to those observed through SEM, were detected by TEM for $\alpha\text{-HfW}_2\text{O}_8$ and the solid solutions; some more micrographs are included in the supplementary information (Figure S3). Well-formed microcrystals with high crystallinity are shown for $\text{Hf}_{0.99}\text{Lu}_{0.01}\text{W}_2\text{O}_{7.995}$ in Figure 7a. The lengths of the microcrystals vary in the range of 2 to 5 μm .

The lattice arrangements, clearly arranged crystalline planes and interplanar distances for the solid solutions $\text{Hf}_{0.99}\text{Lu}_{0.01}\text{W}_2\text{O}_{7.995}$, $\text{Hf}_{0.99}\text{Eu}_{0.01}\text{W}_2\text{O}_{7.995}$, and $\text{Hf}_{0.95}\text{Eu}_{0.05}\text{W}_2\text{O}_{7.975}$ are shown in Figure 7b–d.

The crystal plane alignments in the direction correspondent to the highest XRD diffraction peak in the cubic structure of $\alpha\text{-HfW}_2\text{O}_8$ can be seen. The interplanar distances of the samples $\text{Hf}_{0.95}\text{Eu}_{0.05}\text{W}_2\text{O}_{7.975}$ and $\text{Hf}_{0.99}\text{Lu}_{0.01}\text{W}_2\text{O}_{7.995}$ (220) and (221) show increasing distances for $\text{Hf}_{0.95}\text{Eu}_{0.05}\text{W}_2\text{O}_{7.975}$, which is a result of the bigger ionic radius of Eu^{3+} (94.7 pm Eu^{3+} ; 86.1 pm Lu^{3+} [27]).

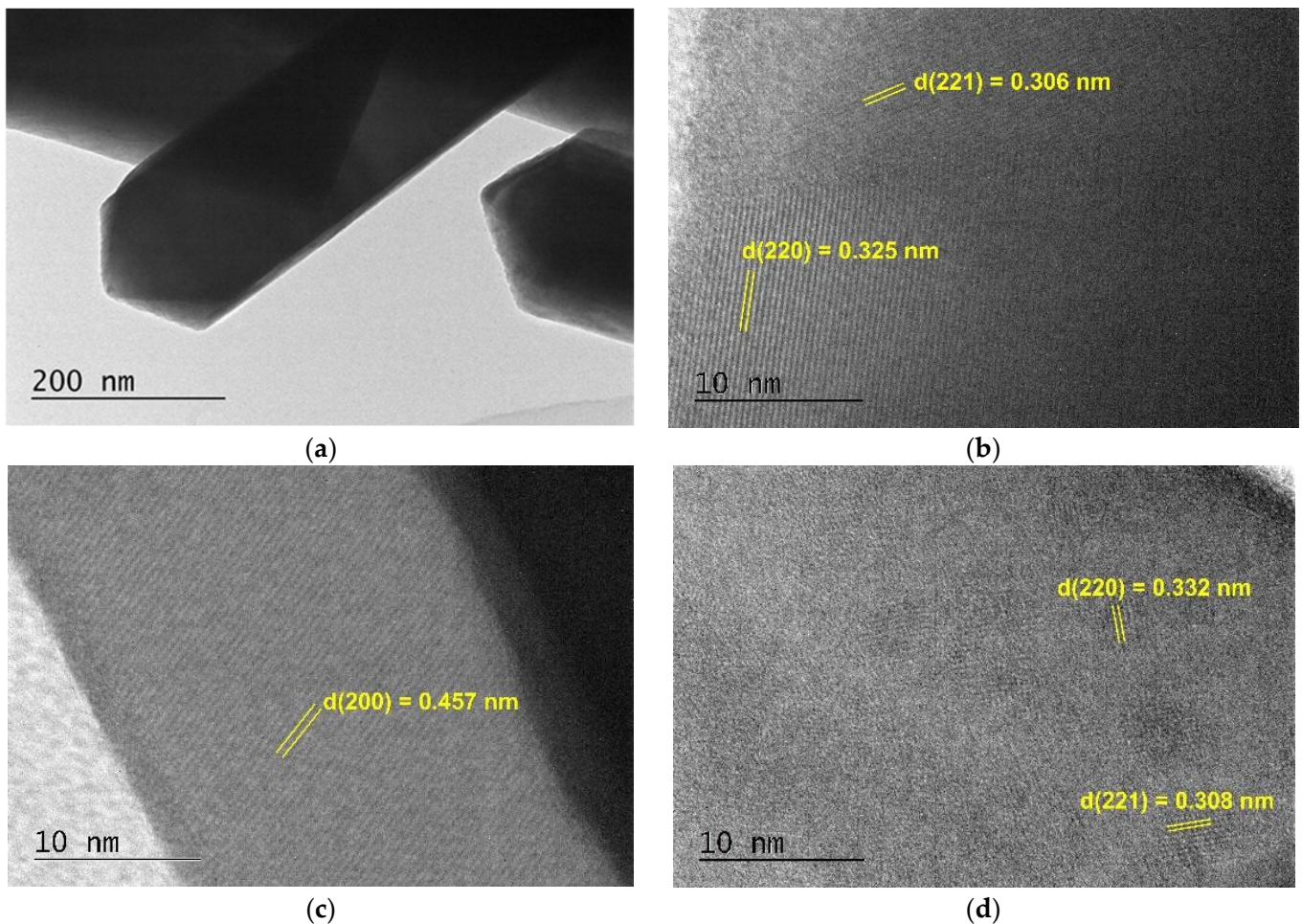


Figure 7. TEM micrographs for (a) microcrystals of $\text{Hf}_{0.99}\text{Tm}_{0.01}\text{W}_2\text{O}_{7.995}$ with well-defined edges, (b) $\text{Hf}_{0.99}\text{Lu}_{0.01}\text{W}_2\text{O}_{7.995}$, (c) $\text{Hf}_{0.99}\text{Eu}_{0.01}\text{W}_2\text{O}_{7.995}$, and (d) $\text{Hf}_{0.95}\text{Eu}_{0.05}\text{W}_2\text{O}_{7.975}$ showing the internal crystalline structure with characteristic interplanar distances.

3.4. Phase Transition; Reversibility; and the Coefficients of Thermal Expansion in the Pure HfW_2O_8 and in the Solid Solutions $\text{Hf}_{1-x}\text{Ln}_x\text{W}_2\text{O}_{8-x/2}$ ($x = 0.01$ and 0.05)

3.4.1. The Phase Transition $\alpha\text{-HfW}_2\text{O}_8$ to $\beta\text{-HfW}_2\text{O}_8$ and its Reversibility

The X-Ray diffraction patterns recorded at 25/250/25 °C of pure HfW_2O_8 synthesized by hydrothermal method are presented in Figure 8, from them, the $\alpha\text{-HfW}_2\text{O}_8 \rightleftharpoons \beta\text{-HfW}_2\text{O}_8$ transition and its reversibility follows. The reflex at 16.9 2Theta diminishes its intensity, while the intensity of the reflex at 31 2Theta diminishes and disappears with the temperature increase (indicated by arrows in Figure 8). As long as the latter two reflexes are typical for $\alpha\text{-HfW}_2\text{O}_8$, their disappearance at 250 °C is a sign of the completed phase transition $\alpha\text{-HfW}_2\text{O}_8 \rightarrow \beta\text{-HfW}_2\text{O}_8$. After cooling down to 25 °C, these reflexes can be detected again as evidence for the reversibility of the transition (Figure 8).

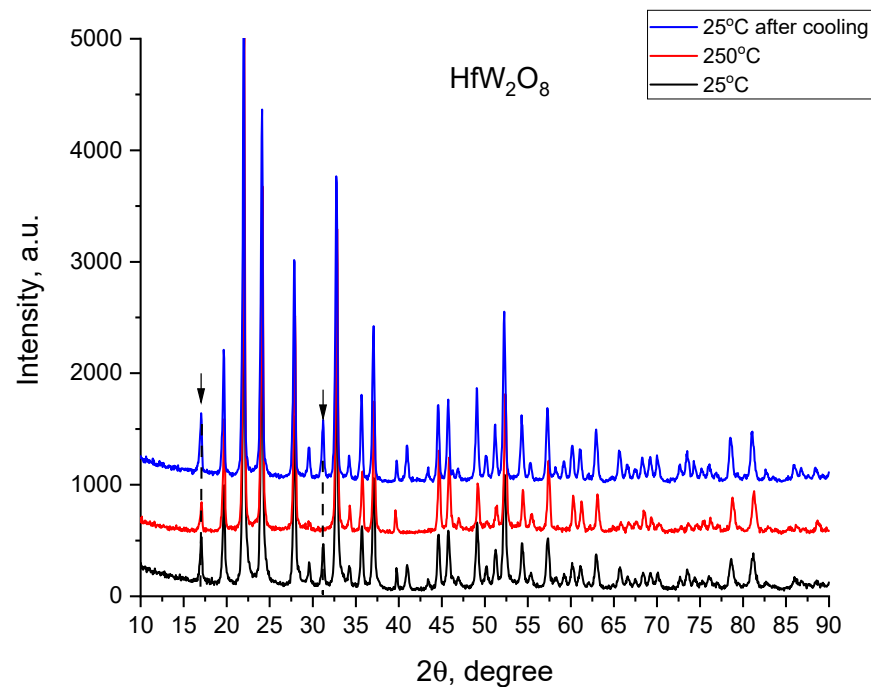


Figure 8. XRD of pure HfW_2O_8 , recorded at 25/250/25 °C (from bottom to top), demonstrating the reversibility of the $\alpha\text{-HfW}_2\text{O}_8 \rightleftharpoons \beta\text{-HfW}_2\text{O}_8$ transition. The reflexes at 16.9 and 31.1 2Theta are indicated.

3.4.2. Unit Cell Parameters and Coefficients of Thermal Expansion (CTE)

The unit cell parameters and the coefficients of thermal expansion (CTE) for pure HfW_2O_8 and $\text{Hf}_{1-x}\text{Ln}_x\text{W}_2\text{O}_{8-x/2}$, $x = 0.01$ and 0.05 , along with the coefficients of thermal expansion (CTE) calculated for the interval 25–100 °C ($\alpha\text{-HfW}_2\text{O}_8$ phase) and 200–250 °C ($\beta\text{-HfW}_2\text{O}_8$ phase) and 25–250 °C are presented in Table 1.

Table 1. Unit cell parameters and CTE for pure HfW_2O_8 and $\text{Hf}_{1-x}\text{Ln}_x\text{W}_2\text{O}_{8-x/2}$ ($x = 0.01$ and 0.05).

	T °C	HfW_2O_8	$\text{Hf}_{1-x}\text{Eu}_x\text{W}_2\text{O}_{8-x/2}$		$\text{Hf}_{1-x}\text{Tm}_x\text{W}_2\text{O}_{8-x/2}$		$\text{Hf}_{1-x}\text{Lu}_x\text{W}_2\text{O}_{8-x/2}$	
			x = 0.01	x = 0.05	x = 0.01	x = 0.05	x = 0.01	x = 0.05
Unit cell parameters, Å	25	9.1244(2)	9.1246(3)	9.1245(1)	9.1245(1)	9.1245(1)	9.1244(1)	9.1243(1)
	100	9.1174(1)	9.1179(1)	9.1177(1)	9.1171(1)	9.1170(1)	9.1173(1)	9.1172(1)
	200	9.1055(1)	9.1058(2)	9.1057(1)	9.1050(3)	9.1049(1)	9.1049(1)	9.1048(1)
	250	9.1050(1)	9.1051(1)	9.1053(2)	9.1044(1)	9.1046(1)	9.1044(1)	9.1045(2)
CTE, $\times 10^{-6} \text{ K}^{-1}$	25–100	−10.22	−9.79	−9.94	−10.81	−10.96	−10.38	−10.36
	200–250	−1.10	−1.54	−0.87	−1.32	−0.66	−1.10	−0.66
	25–250	−9.45	−9.49	−9.35	−9.79	−9.69	−9.74	−9.64

Considering that HfW_2O_8 solid solutions have isotropic negative thermal expansion, we used the classical formula for linear expansion (instead of volume expansion) [14]

$$\Delta a = \alpha a_{298} \Delta T,$$

where Δa is the change in the unit cell parameter, α is the linear coefficient of thermal expansion, a_{298} is the unit cell parameter at room temperature, and ΔT is the change in the temperature.

It can be seen that the cubic unit-cell parameter for pure HfW_2O_8 in fact diminishes with the temperature increase from 25 to 250 °C, proving that the cell shrinks and demonstrating the negative coefficient of thermal expansion. The same tendency is observed

for the unit cell parameters of $\text{Hf}_{0.99}\text{Ln}_{0.01}\text{W}_2\text{O}_{8-x/2}$ and $\text{Hf}_{0.95}\text{Ln}_{0.05}\text{W}_2\text{O}_{8-x/2}$, upon the temperature increase (Table 1). When the Ln^{3+} content increases from $x = 0.01$ to $x = 0.05$, an influence on the unit cell parameters is observed; this influence is well pronounced for Eu^{3+} , i.e., a slight decrease for the low-temperature phase $\alpha\text{-Hf}_{1-x}\text{Ln}_x\text{W}_2\text{O}_{8-x/2}$ (25 °C) and a slight increase for the high temperature phase $\beta\text{-Hf}_{1-x}\text{Ln}_x\text{W}_2\text{O}_{8-x/2}$ (250 °C) (within the error range). In comparison with the pure HfW_2O_8 , an increase of the cubic unit-cell parameter of $\text{Hf}_{1-x}\text{Ln}_x\text{W}_2\text{O}_{8-x/2}$ is noticeable, especially for the Eu^{3+} -containing samples (Table 1), as result of the bigger Eu^{3+} ion.

The coefficients of thermal expansion calculated were -10.22 and $-1.10 \times 10^{-6} \text{ K}^{-1}$, for the pure $\alpha\text{-HfW}_2\text{O}_8$ and $\beta\text{-HfW}_2\text{O}_8$ phases, respectively (Table 1). They differ from the literature data, $-9 \times 10^{-6} \text{ K}^{-1}$ and $-6 \times 10^{-6} \text{ K}^{-1}$ [11], quite likely as a result of the different method used for synthesis. The presence of Ln^{3+} in the solid solutions is essential for the $\alpha\text{-HfW}_2\text{O}_8$ phase to effect an increase of CTE, and for $\beta\text{-HfW}_2\text{O}_8$ phase, to effect a decrease of CTE when a Ln^{3+} increase is observed. For the low temperature, the $\alpha\text{-Hf}_{1-x}\text{Ln}_x\text{W}_2\text{O}_{8-x/2}$ phase (25–100 °C) CTE increases with Ln^{3+} especially for Eu^{3+} - and Tm^{3+} -containing samples. The CTE values for the high-temperature phase $\beta\text{-Hf}_{0.95}\text{Ln}_{0.05}\text{W}_2\text{O}_{8-x/2}$ (200–250 °C) are lower than the value for the pure high-temperature $\beta\text{-HfW}_2\text{O}_8$ phase.

The high-temperature XRD values for $\text{Hf}_{1-x}\text{Ln}_x\text{W}_2\text{O}_{8-x/2}$ ($x = 0.01$; $\text{Ln} = \text{Eu}, \text{Lu}$) show that the temperature of 140 °C is a critical temperature for the phase transition, i.e., the reflex at 31 2Theta, typical for $\alpha\text{-HfW}_2\text{O}_8$, disappears there (Figure 9a,b).

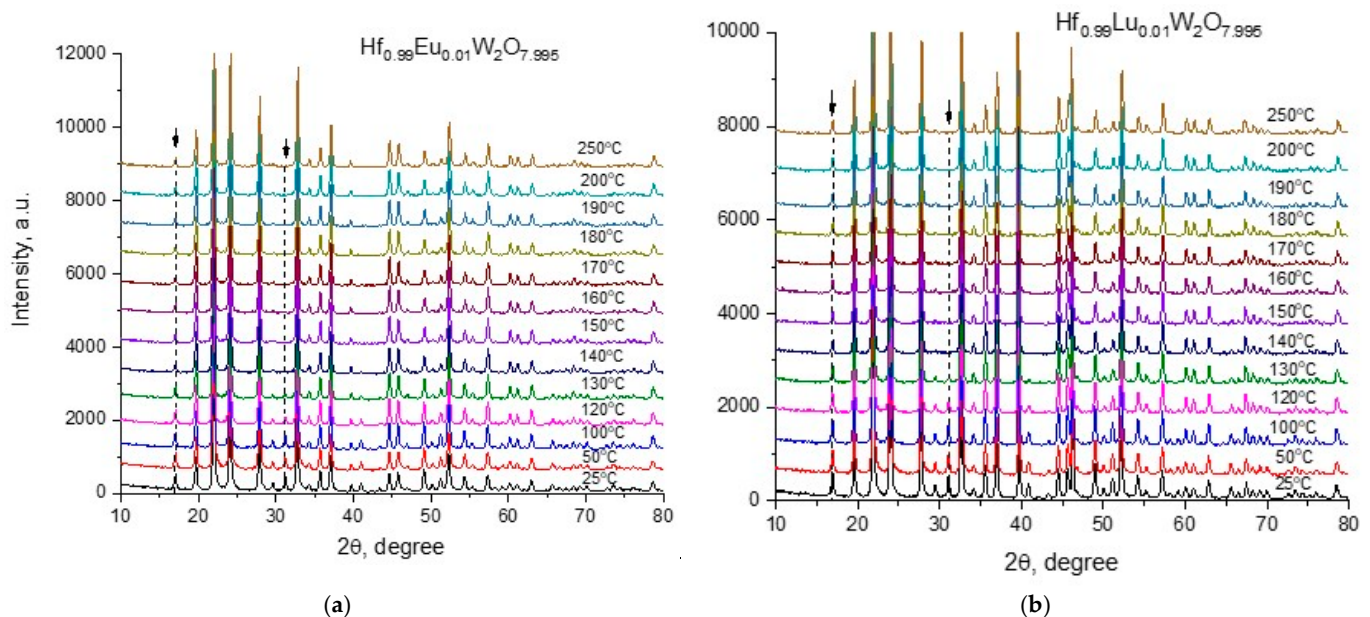


Figure 9. High temperature XRD for $\text{Hf}_{1-x}\text{Ln}_x\text{W}_2\text{O}_{8-x/2}$, $x = 0.01$; Ln (a) Eu, (b) Lu. The temperature of 140 °C is the critical temperature of the phase transition.

3.4.3. Order-to-Disorder Phase Transition for $\text{Hf}_{1-x}\text{Ln}_x\text{W}_2\text{O}_{8-x/2}$ ($x = 0.01$; 0.05) and the Role of Ln^{3+}

The structure of the low-temperature $\alpha\text{-HfW}_2\text{O}_8$ and $\beta\text{-HfW}_2\text{O}_8$ phase has corner-sharing HfO_6 octahedra and WO_4 tetrahedra. The difference concerns the WO_4 tetrahedra, namely, in the $\alpha\text{-HfW}_2\text{O}_8$ phase, each WO_4 tetrahedron shares three of its oxygen atoms with the adjacent octahedra, while, in the high-temperature $\beta\text{-HfW}_2\text{O}_8$ phase, two WO_4 share three joined O atoms. The crystal structures of the low-temperature $\alpha\text{-Hf}_{1-x}\text{Ln}_x\text{W}_2\text{O}_{8-x/2}$ and the high-temperature $\beta\text{-Hf}_{1-x}\text{Ln}_x\text{W}_2\text{O}_{8-x/2}$ are shown in Figure 10, where the half-filled WO_4 in $\beta\text{-Hf}_{1-x}\text{Ln}_x\text{W}_2\text{O}_{8-x/2}$ are accentuated by color.

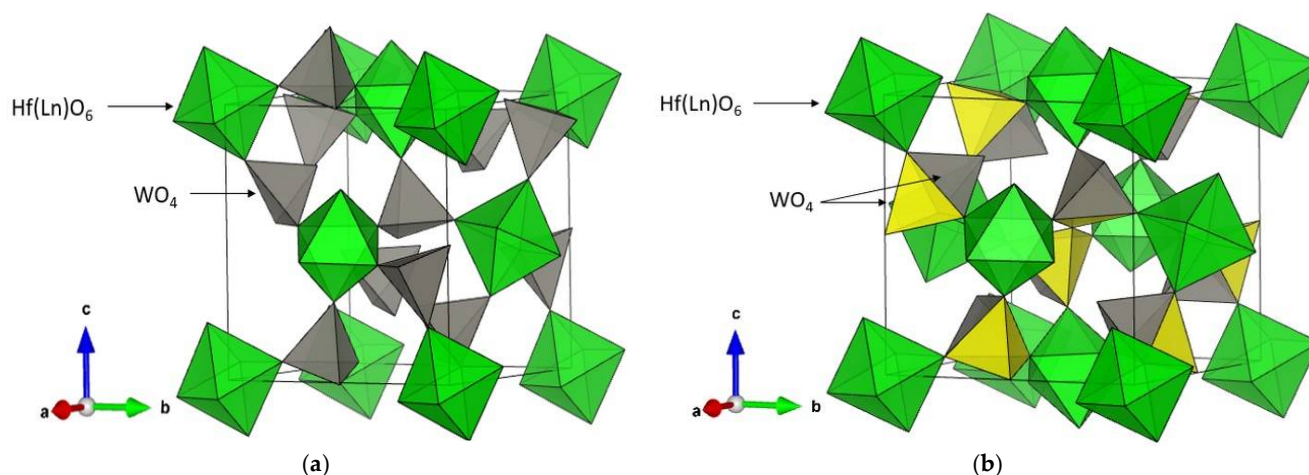


Figure 10. Crystal structures of (a) $\alpha\text{-Hf}_{1-x}\text{Ln}_x\text{W}_2\text{O}_{8-x/2}$ and (b) $\beta\text{-Hf}_{1-x}\text{Ln}_x\text{W}_2\text{O}_{8-x/2}$. The yellow and grey tetrahedra in $\beta\text{-Hf}_{1-x}\text{Ln}_x\text{W}_2\text{O}_{8-x/2}$ represent the half-filled WO_4 .

The orientations of the WO_4 tetrahedra determine the transition of $\alpha\text{-HfW}_2\text{O}_8 \rightarrow \beta\text{-HfW}_2\text{O}_8$, which is called order-to-disorder phase transition [8]. The extent of the WO_4 tetrahedra disorder depending on the temperature can be evaluated by the parameter η_T' [20], calculated by the following equation:

$$\eta_T' = \sqrt{\frac{\left[\left(\frac{I_{310}}{I_{210}}\right)\right]_T}{\left[\left(\frac{I_{310}}{I_{210}}\right)_{\text{HfW}_2\text{O}_8}\right]_{298\text{K}}}},$$

where I_{310} and I_{210} are the integrated intensities of the reflections (310) and (210), respectively; the former indicates the ordered $\alpha\text{-HfW}_2\text{O}_8$ phase, the latter does not change during the phase transition. As can be seen in Figure 11, the relative order parameter at room temperature significantly decreases when Eu^{3+} is introduced to the system, leading to a higher degree of distortion in $\text{Hf}_{0.99}\text{Eu}_{0.01}\text{W}_2\text{O}_{8-x/2}$. The effect of Tm^{3+} and Lu^{3+} on $\text{Hf}_{0.99}\text{Ln}_{0.01}\text{W}_2\text{O}_{8-x/2}$ is less pronounced, and it can be explained by the degree of solid solubility of the heavier Ln^{3+} , which is much more soluble in the system due to the smaller ionic radii in comparison with Hf^{4+} radius (Lu^{3+} 86.1, Tm^{3+} 88.0, Eu^{3+} 94.7, Hf^{4+} 71 pm, CN 6 [27]).

3.5. UV–Vis Absorption of the Solid Solutions and the Energy of the Band Gaps

The absorbance in the UV–Vis range (200–450 nm) shows a clear maximum at approximately 250 nm for all samples. A weak absorbance at approximately 400 nm differs $\text{Hf}_{1-x}\text{Tm}_x\text{W}_2\text{O}_8$ ($x = 0.01$ and 0.05) from the other samples (Figure 12a). It is quite likely that the bands between 250 and 350 nm exist due to the strong ligand-to-metal charge transfer observed both in slightly distorted monotungstate structures and polytungstates [28].

Band-gap-energy calculations were accomplished based on UV–Vis data (Figure 12a,b) and listed in Table 2. The UV–Vis data were analyzed to determine the relationship among the optical band gap, absorption coefficient, and energy ($h\nu$) of the incident photon for near-edge optical absorption. The calculations were performed from the measured curves by fits according to Tauc's equation [29]; i.e., $\alpha h\nu = A(h\nu - E_g)^n$, where A is a constant independent of $h\nu$, E_g is the band gap, and n depends on the type of transition. In addition, the well-known approach for E_g determination from the intersection of the linear fits of $(\alpha h\nu)^{1/n}$ versus $h\nu$ on the x -axis was used, n being $1/2$ and 2 for direct and indirect band gaps, respectively.

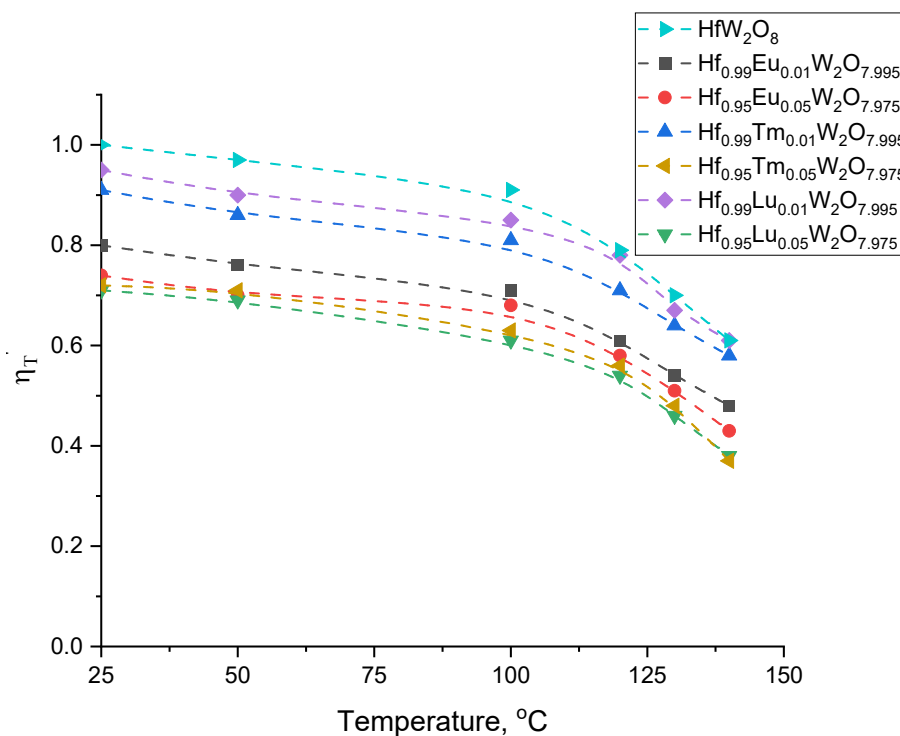


Figure 11. Influence of the temperature and amount of Ln(III) in the solid solutions $\text{Hf}_{1-x}\text{Ln}_x\text{W}_2\text{O}_{8-x/2}$ ($x = 0.01$ and 0.05) on WO_4 tetrahedra disorder.

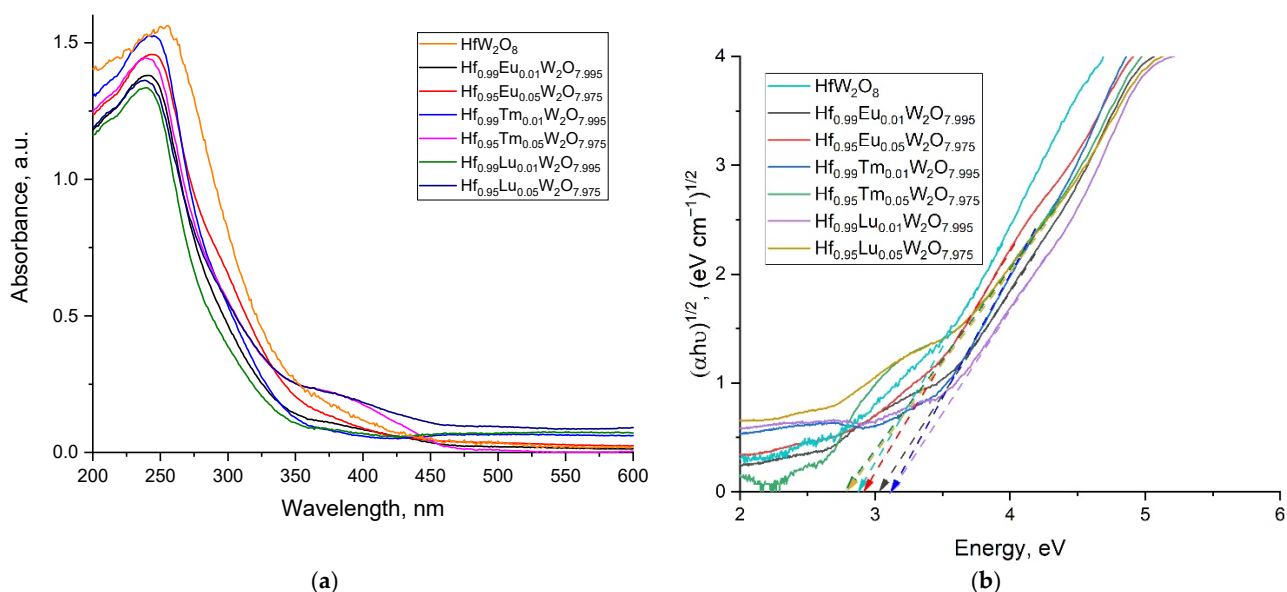


Figure 12. (a) UV-Vis spectra and (b) Energy of the band gap.

The band gap value of the pure $\alpha\text{-HfW}_2\text{O}_8$, 2.87 eV, obtained by the Tauc's equation corresponds well to the value observed by Ouyang for pure $\alpha\text{-ZrW}_2\text{O}_8$, 2.84 eV [30]. The values of the solid solutions for all samples of the type $\text{Hf}_{0.99}\text{Ln}_{0.01}\text{W}_2\text{O}_{8-x/2}$ increased in the range of 3.02, 3.10, and 3.12 eV, for Eu^{3+} , Tm^{3+} , and Lu^{3+} , respectively. This can be attributed to the decrease of the crystallites due to the presence of Ln^{3+} [31]. Interestingly, the further incorporation of Ln^{3+} for $\text{Hf}_{0.95}\text{Ln}_{0.05}\text{W}_2\text{O}_{8-x/2}$ leads to the significant narrowing of the band gap, especially for Tm^{3+} and Lu^{3+} (2.78 eV), most likely due to the increased order of distortion of the WO_4 polyhedra. A similar effect was observed by Muthu and coauthors [32] due to pressure induced amorphization.

Table 2. Energy band gap of the samples, eV.

Nº	Sample	Band Gap E_g , eV
1	α -HfW ₂ O ₈	2.87
2	α -ZrW ₂ O ₈	2.84 [31]
3	Hf _{0.99} Eu _{0.01} W ₂ O _{7.995}	3.02
4	Hf _{0.95} Eu _{0.05} W ₂ O _{7.975}	2.92
5	Hf _{0.99} Tm _{0.01} W ₂ O _{7.995}	3.10
6	Hf _{0.95} Tm _{0.05} W ₂ O _{7.975}	2.78
7	Hf _{0.99} Lu _{0.01} W ₂ O _{7.995}	3.12
8	Hf _{0.95} Lu _{0.05} W ₂ O _{7.975}	2.78

4. Conclusions

Using the hydrothermal method, pure HfW₂O₈- and Ln³⁺-containing homogeneous solid solutions Hf_{1-x}Ln_xW₂O_{8-x/2} ($x = 0.01, 0.05$; Ln = Eu, Tm, Lu) were obtained and characterized by XRD, Raman, FT-IR spectroscopy, and electron microscopy. The influence of Ln³⁺ was detected by (i) the Raman spectra shifting to the higher wavenumbers of the most intensive bands of Hf_{1-x}Ln_xW₂O_{8-x/2}; (ii) the unit cell parameters decreasing with the temperature for the solid solutions Hf_{1-x}Ln_xW₂O_{8-x/2} in connection with the isotropic negative thermal expansion; (iii) the observed increase of CTE for the α -HfW₂O₈ phase and the decrease of CTE for the β -HfW₂O₈ phase, with a Ln³⁺ increase; (iv) the increased energy-band-gap values of the solid solutions Hf_{0.99}Ln_{0.01}W₂O_{8-x/2} with decreases in the atomic radii of Eu³⁺, Tm³⁺, and Lu³⁺; and (v) the significant narrowing of the band gap for Hf_{0.95}Ln_{0.05}W₂O_{8-x/2} (Ln = Tm³⁺ and Lu³⁺) due to the increased order of distortion of the WO₄ polyhedra.

The question for the potential incorporation of Ln³⁺ into the structure of the tungstates is interesting taking into account the options for the potential position of the Ln³⁺, i.e., either in the interstices or on the surface or by replacing the Hf⁴⁺ ions in the HfO₆ octahedra. This is challenging due to the fact that hafnium and lanthanides possess different atomic and ionic radii, complicating the replacement of Hf⁴⁺/Ln³⁺. On the other hand, the differences between the typical oxidation states of lanthanides and hafnium, +3 and +4, respectively, leads to the question of the neutrality of the charge of the solid solutions formed, which makes it important to follow the oxygen vacancies. In spite of the Rietveld refinement of the occupancy of all oxygen atoms, due to the very low concentration of defects, major deviations were not detected.

Supplementary Materials: The following supporting information can be downloaded at: <https://www.mdpi.com/article/10.3390/cryst12030327/s1>, Figure S1: FT-IR spectra of the samples in the range of 4000–400 cm⁻¹; Figure S2: TEM micrographs; Figure S3: SEM micrographs; Table S1: Starting structural parameters for α -HfW₂O₈; Table S2: Parameters for the starting model for β -HfW₂O₈, based on [22]; Table S3: Raman spectra of HW₂O₈ and Hf_{1-x}Ln_xW₂O_{8-x/2} ($x = 0.01$ and 0.05): values of the bands position of the samples.

Author Contributions: Conceptualization, M.T. and M.M.; methodology, M.T.; software, M.T.; validation, M.T. and M.N.; formal analysis, M.T. and E.V.; investigation, M.T.; resources, M.T.; writing—original draft preparation, M.M. and M.T.; writing—review and editing, M.M. and M.T.; supervision, M.T.; project administration, M.T. All authors have read and agreed to the published version of the manuscript.

Funding: Bulgarian Fund for Scientific Investigations, project DM 19/5; European Regional Development Fund within the Operational Programme “Science and Education for Smart Growth 2014–2020” under the Project CoE “National Center of Mechatronics and Clean Technologies” BG05M2OP001-1.001-0008-C01.

Institutional Review Board Statement: Not applicable.

Informed Consent Statement: Not applicable.

Data Availability Statement: Not applicable.

Acknowledgments: The financial support from the Bulgarian Fund for Scientific Investigations, project DM 19/5 from 2017 is highly acknowledged. E.V. acknowledges the support of the European Regional Development Fund within the Operational Programme “Science and Education for Smart Growth 2014–2020” under the Project CoE “National Center of Mechatronics and Clean Technologies” BG05M2OP001-1.001-0008-C01.

Conflicts of Interest: The authors declare no conflict of interest.

References

1. Takenaka, K. Negative thermal expansion materials: Technological key for control of thermal expansion. *Sci. Technol. Adv. Mater.* **2012**, *13*, 013001. [\[CrossRef\]](#) [\[PubMed\]](#)
2. Lind, C. Two decades of negative thermal expansion research: Where do we stand? *Materials* **2012**, *5*, 1125–1154. [\[CrossRef\]](#) [\[PubMed\]](#)
3. Sanson, A.; Chen, J. Towards the control of thermal expansion: From 1996 to today. *Front. Chem.* **2019**, *7*, 284. [\[CrossRef\]](#) [\[PubMed\]](#)
4. Evans, D.L.; Fischer, G.R.; Geiger, J.E.; Martin, F.W. Thermal expansions and chemical modifications of cordierite. *J. Am. Ceram. Soc.* **1980**, *63*, 629–634. [\[CrossRef\]](#)
5. Phillips, A.E.; Goodwin, A.L.; Halder, G.J.; Southon, P.D.; Kepert, C.J. Nanoporosity and exceptional negative thermal expansion in single-network cadmium cyanide. *Angew. Chem.* **2008**, *120*, 1418–1421. [\[CrossRef\]](#)
6. Azuma, M.; Chen, W.-T.; Seki, H.; Czapski, M.; Smirnova, O.; Oka, K.; Mizumaki, M.; Watanuki, T.; Ishimatsu, N.; Kawamura, N.; et al. Colossal negative thermal expansion in BiNiO₃ induced by intermetallic charge transfer. *Nat. Commun.* **2011**, *2*, 347. [\[CrossRef\]](#)
7. Shi, N.; Song, Y.; Xing, X.; Chen, J. Negative thermal expansion in framework structure materials. *Coord. Chem. Rev.* **2021**, *449*, 214204. [\[CrossRef\]](#)
8. Evans, J.S.; Mary, T.A.; Vogt, T.; Subramanian, M.A.; Sleight, A.W. Negative thermal expansion in ZrW₂O₈ and HfW₂O₈. *Chem. Mater.* **1996**, *8*, 2809–2823. [\[CrossRef\]](#)
9. Evans, J.S.O.; David, W.I.F.; Sleight, A.W. Structural investigation of the negative thermal expansion material ZrW₂O₈. *Acta Cryst.* **1999**, *B55*, 333–340. [\[CrossRef\]](#)
10. Mary, T.A.; Evans, J.S.O.; Vogt, T.; Sleight, A.W. Negative thermal expansion from 0.3 to 1050 Kelvin in ZrW₂O₈. *Science* **1996**, *272*, 90–92. [\[CrossRef\]](#)
11. Gallington, L.C.; Chapman, K.W.; Morelock, C.R.; Chupas, P.J.; Wilkinson, A.P. Dramatic softening of the negative thermal expansion material HfW₂O₈ upon heating through its WO₄ orientational order-disorder phase transition. *J. Appl. Phys.* **2014**, *115*, 053512. [\[CrossRef\]](#)
12. Yamamura, Y.; Nakajima, N.; Tsuji, T. Calorimetric and X-ray diffraction studies of a-to-b structural phase transitions in HfW₂O₈ and ZrW₂O₈. *Phys. Rev. B* **2001**, *64*, 184109. [\[CrossRef\]](#)
13. Yamamura, Y.; Nakajima, N.; Tsuji, T.; Koyano, M.; Iwasa, Y.; Saito, K.; Sorai, M. Heat capacity and Grüneisen function of negative thermal expansion compound HfW₂O₈. *Solid State Commun.* **2002**, *121*, 213–217. [\[CrossRef\]](#)
14. Encheva, E.D.; Nedyalkov, M.K.; Tsvetkov, M.P.; Milanova, M.M. The influence of the modification of zirconium tungstate with Eu(III) on the $\alpha \rightarrow \beta$ phase transition temperature and optical band gap. *Bulg. Chem. Comm. Spec. Issue F* **2018**, *50*, 143–149.
15. De Meyer, C.; Bouree, F.; Evans, J.S.O.; de Buysser, K.; Bruneel, E.; van Driessche, I.; Hoste, S. Structure and phase transition of Sn-substituted Zr_{1-x}Sn_xW₂O₈. *J. Mater. Chem.* **2004**, *14*, 2988–2994. [\[CrossRef\]](#)
16. De Buysser, K.; van Driessche, I.; Putte, B.V.; Vanhee, P.; Schaubroeck, J.; Hoste, S. Study of negative thermal expansion and shift in phase transition temperature in Ti⁴⁺- and Sn⁴⁺-substituted ZrW₂O₈ materials. *Inorg. Chem.* **2008**, *47*, 736–741. [\[CrossRef\]](#)
17. Yamamura, Y.; Masago, K.; Kato, M.; Tsuji, T. Comprehensive interpretation of a substitution effect on an order-disorder phase transition in A_{1-x}M_xW₂O_{8-y} (A = Zr, Hf; M = trivalent cations) and other ZrW₂O₈-based solid solutions. *J. Phys. Chem. B* **2007**, *111*, 10118–10122. [\[CrossRef\]](#) [\[PubMed\]](#)
18. Yamamura, Y.; Nakajima, N.; Tsuji, T.; Kojima, A.; Kuroiwa, Y.; Sawada, A.; Aoyagi, S.; Kasatani, H. Drastic lowering of the order-disorder phase transition temperatures in Zr_{1-x}M_xW₂O_{8-y} (M = Sc, Y, In) solid solutions. *Phys. Rev. B* **2004**, *70*, 104107. [\[CrossRef\]](#)
19. Nakajima, N.; Yamamura, Y.; Tsuji, T. Synthesis and physical properties of negative thermal expansion materials Zr_{1-x}M_xW₂O_{8-y} (M = Sc, In, Y) substituted for Zr(IV) sites by M(III) ions. *Solid State Commun.* **2003**, *128*, 193–196. [\[CrossRef\]](#)
20. Li, H.-H.; Han, J.-S.; Ma, H.; Huang, L.; Zhao, X.-H. Zr_{1-x}Ln_xW₂O_{8-x/2} (Ln = Eu, Er, Yb): Solid solutions of negative thermal expansion-synthesis, characterization and limited solid solubility. *J. Solid State Chem.* **2007**, *180*, 852–857. [\[CrossRef\]](#)
21. Rodriguez-Carvajal, J. Recent developments of the program fullprof. In *Newsletter in Commission on Powder Diffraction*; IUCr: Chester, UK, 2001; Volume 26, pp. 12–19.
22. Kameswari, U.; Sleight, A.W.; Evans, J.S. Rapid synthesis of ZrW₂O₈ and related phases, and structure refinement of ZrW₂MoO₈. *Int. J. Inorg. Mater.* **2000**, *2*, 333–337. [\[CrossRef\]](#)
23. Thummavichai, K.; Wang, N.; Xu, F.; Rance, G.; Xia, Y.; Zhu, Y. In situ investigations of the phase change behavior of tungsten oxide nanostructures. *R. Soc. Open Sci.* **2018**, *5*, 171932. [\[CrossRef\]](#) [\[PubMed\]](#)

24. Yamamura, Y.; Nakajima, N.; Tsuji, T.; Koyano, M.; Iwasa, Y.; Katayama, S.; Saito, K.; Sorai, M. Low-temperature heat capacities and Raman spectra of negative thermal expansion compounds ZrW_2O_8 and HfW_2O_8 . *Phys. Rev. B* **2002**, *66*, 014301. [[CrossRef](#)]
25. Jorgensen, J.D.; Hu, Z.; Shor, S.; Sleight, A.W.; Evans, J.S.O. Pressure-induced cubic-to-orthorhombic phase transformation in the negative thermal expansion material HfW_2O_8 . *J. Appl. Phys.* **2001**, *89*, 3184–3188. [[CrossRef](#)]
26. Chen, B.; Muthu, D.V.S.; Liu, Z.X.; Sleight, A.W.; Kruger, M.B. High-pressure Raman and infrared study of HfW_2O_8 . *Phys. Rev. B* **2001**, *64*, 214111. [[CrossRef](#)]
27. Shannon, R.D. Revised effective ionic radii and systematic studies of interatomic distances in halides and chalcogenides. *Acta Cryst.* **1976**, *A32*, 751–767. [[CrossRef](#)]
28. Ross-Medgaarden, E.I.; Wachs, E.I. Structural determination of bulk and surface tungsten oxides with UV-vis diffuse reflectance spectroscopy and Raman spectroscopy. *J. Phys. Chem. C* **2007**, *111*, 15089–15099. [[CrossRef](#)]
29. Tauc, J.; Grigorovici, R.; Vancu, A. Optical properties and electronic structure of amorphous germanium. *Phys. Status Solidi B* **1966**, *15*, 627–637. [[CrossRef](#)]
30. Ouyang, L.; Xu, Y.-N.; Ching, W.Y. Electronic structure of cubic and orthorhombic phases of ZrW_2O_8 . *Phys. Rev. B* **2002**, *65*, 113110. [[CrossRef](#)]
31. Church, J.S.; Cant, N.W.; Trimm, D.L. Stabilisation of aluminas by rare earth and alkaline earth ions. *Appl. Catal.* **1993**, *101*, 105. [[CrossRef](#)]
32. Muthu, D.V.S.; Chen, B.; Sleight, A.W.; Wrobel, J.M.; Kruger, M.B. ZrW_2O_8 and HfW_2O_8 : Band gap shifts under pressure. *Solid State Commun.* **2002**, *122*, 25–28. [[CrossRef](#)]